Soft Matter

PAPER

View Article Online
View Journal | View Issue

Check for updates

Cite this: *Soft Matter*, 2025, **21**, 8025

Interfacial healing driven by wetting of nanoparticle films

Claire Hotton, *[ab] Jean-Philippe Renault[b] and Ludovic Pauchard *[a]

During the drying of colloidal coatings, stress release can induce mechanical instabilities that often unfold in successive stages. In particular, crack-limited fragments may partially delaminate from the substrate, forming distinct adhesion zones. This delamination process results from a complex interplay between capillary forces, internal stresses, and interfacial adhesion. While often seen as irreversible, recent findings reveal that delamination can, under certain conditions, exhibit partial reversibility. This discovery opens promising avenues for developing self-healing coatings. In this study, we investigate the reversible delamination of transparent silica nanoparticle films subjected to cyclic drying and rewetting. The transparency of the films allows for accurate mapping of delaminated and adhered regions before and after imbibition. Upon rewetting, swelling induces fragment flattening and re-adhesion to the substrate. As drying resumes, new delamination patterns emerge, comparable in size but located differently, indicating interfacial healing during the wetting phase. These results provide key insights into reversible adhesion mechanisms and contribute to the design of more resilient and adaptive coatings under fluctuating environmental conditions.

Received 23rd July 2025,
Accepted 30th September 2025

DOI: 10.1039/d5sm00750j

rsc.li/soft-matter-journal

Open Access Article. Published on 30 2025. Downloaded on 22/11/25 23:07:05.
This article is licensed under a Creative Commons Attribution 3.0 Unported Licence.

1. Introduction

The delamination of colloidal solid films induced by drying is a complex phenomenon that has attracted considerable attention in soft matter and materials science. This process arises from the interplay between capillary forces, evolving mechanical stresses, and adhesion to the substrate. As drying proceeds, the buildup of internal stress can drive a variety of instabilities, leading to the emergence of characteristic patterns such as cracks,[1–3] blisters,[4] or polygonal delaminations.[5] These patterns not only reflect the dynamics of the drying process but also offer insights into the mechanical properties of the film and its coupling with the underlying substrate.

While delamination is commonly regarded as an irreversible failure mode, especially in brittle colloidal films where mechanical rupture dominates. However, recent observations suggest that for colloidal films that are not excessively brittle, for instance, aged films with reduced fragility, delamination can exhibit a degree of reversibility. This reversibility opens intriguing possibilities for understanding and manipulating the adhesion dynamics between the film and the substrate. By identifying the underlying causes of delamination during drying and implementing effective healing strategies, it becomes possible to develop coatings that not only resist delamination but also have the ability to autonomously repair themselves if delamination occurs. This is crucial for applications like protective coatings, sensors, flexible electronics, and biomedical devices, where mechanical stability under varying humidity or temperature is essential. While reversible delamination can compromise performance if uncontrolled, it can also enable self-healing or adaptive surfaces. In cleaning technologies, it may help lift contaminants without damaging substrates, by leveraging hydration-induced detachment.[6] In such contexts, the ability to predict, control, and reverse delamination processes contributes to improve the performance and reliability of next-generation soft materials and devices.

In this study, we aim to investigate the reversibility of delamination in colloidal films during cyclic processes of drying and imbibition. Specifically, we focus on films that have undergone partial delamination, forming characteristic polygonal patterns. These films under study are composed of silica nanoparticles and develop cracks during the drying process. The transparency of the resulting fragments allows for the observation and quantification of adhered and delaminated regions using optical microscopy. Rewetting such a film with water induces swelling and flattening the fragments[7,8] (Fig. 1). This process results in re-establishing contact with the substrate. However, as drying resumes, the film contracts, and the previously healed regions may again experience stress concentrations, leading to renewed fragment detachment.

[a] *Université Paris-Saclay, CNRS, FAST, 91405, Orsay, France. E-mail: ludovic.pauchard@cnrs.fr*
[b] *Address, LIONS, NIMBE, CEA, CNRS, Université Paris-Saclay, CEA Saclay, Gif-sur-Yvette, France. E-mail: claire.hotton@universite-paris-saclay.fr*

Open Access Article. Published on 30 2025. Downloaded on 22/11/25 23:07:05.
This article is licensed under a Creative Commons Attribution 3.0 Unported Licence.

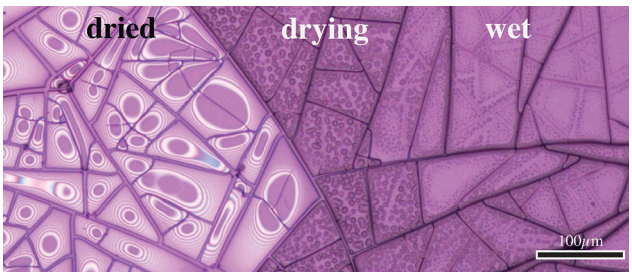

Fig. 1 Optical microscopy image under reflected light on a film of nanosilica (Ludox HS40), 20 ± 5 μm thick. Left region: partially delaminated silica nanoparticle film. Due to the film's transparency, delaminated zones appear with interference fringes, while darker areas correspond to regions still adhering to the substrate. Right region: the film was locally wetted by a deposited water droplet. Upon evaporation, microdroplets formed on the fragmented film, particularly in the central area labeled 'drying'. In the lower region labeled 'wet', water imbibition into the porous film induced a noticeable swelling response.

The resulting adhesion patterns are similar in size but appear in different locations, suggesting interfacial healing during the wetting phase. This behavior highlights a dynamic interplay between the films mechanical properties and the adhesive forces at the film-substrate interface.

2. Experimental

2.1. Colloidal systems

Experiments were performed using various aqueous dispersions of nanosilica particles with well-controlled properties, including particle radius r_p, volume fraction ϕ_0, and a typical polydispersity index below 0.16. The dispersions studied included Ludox SM30 (r_p = 3 ± 1 nm, ϕ_0 = 0.24), Ludox HS40 (r_p = 7 ± 2 nm, ϕ_0 = 0.22), and Ludox TM50 (r_p = 12 ± 2 nm, ϕ_0 = 0.20), all purchased from Sigma-Aldrich. At pH ∼ 9, the silica particles bear a negative surface charge, and in the absence of evaporation, the dispersion stability is primarily governed by electrostatic repulsion. Systematic investigations were primarily carried out using Ludox HS40, due to its superior long-term stability. This was confirmed by rheological measurements performed over several weeks on the same sample, which showed negligible changes in mechanical response.

2.2. Coating formation

The substrates are microscope glass slides carefully cleaned with pure water and then with ethanol before being dried in a heat chamber at 100 °C. The wetting behavior of a water droplet deposited on the substrate provides a way to estimate the surface energy, γ_s, of the surface onto which the colloidal solution is applied. Hence, the surface energy can be deduced from the Dupre formula which relates the surface tension of a liquid drop γ_l and the static contact angle θ_0: $\gamma_s = \gamma_l(1 + \cos\theta_0)$.[9] Based on the water contact angle measurement (22° ± 3°), we estimate the surface energy of the glass substrate at 67 ± 2 mN m^{-1}.

A volume of the colloidal solution is deposited at the surface of the substrate. The solution is then spread across by a steel bar coater exhibiting a gap clearance of 5 μm and 10 μm. This last determines the thickness of the deposited film. The film applicator leaves a liquid film when the bar is moved gently and manually in a single direction.

At this stage, the thickness of the liquid film is not precisely measured but the dry coating is. Since the film surface is exposed to air evaporation of the water starts as soon as the film is applied. Evaporation is carried out at room temperature (20 ± 2 °C) and humidity rate RH = 55 ± 5%. Under these conditions, the transfer of water in the air is limited by diffusion in the surrounding air. The drying/rewetting cycle conducted under these slightly varying ambient conditions yielded reproducible results. Observation is performed using a DM2500 Leica optical microscope with objective 5×, 10× and 50× magnifications for global view and close-up view (envelope thickness measurements), respectively. The thickness of the dry coating, denoted by h, is estimated by differential focus at the film/substrate and film/air interfaces using 50× magnification. This allows for the accuracy of ±2 μm.

During the drying of a colloidal silica film on a glass substrate, capillary bridges can significantly contribute to the adhesion between the gel and the substrate. In the intermediate drying stages, when the film still contains liquid, menisci formed at the particle–substrate and particle–particle interfaces generate capillary forces that pull the particles toward each other and toward the substrate. These forces enhance the contact between the colloidal network and the substrate, promoting stronger adhesion. Although the capillary bridges disappear upon complete drying, their effect persists through increased van der Waals interactions and hydrogen bonding due to the improved conformal contact established during drying. Thus, while capillary forces are transient, they play a crucial role in setting the final adhesion energy by shaping the microstructure and contact quality at the film–substrate interface.

2.3. Measurement of the mechanical properties of drying films

The mechanical properties are characterized using indentation testing with a nanoindenter (Anton Paar). Measurements are performed on planar drying layers deposited on rigid glass slide substrates. These measurements are characterized for three different film thicknesses, h, and at various stages during the drying process. The indentation method involved a fixed penetration depth, p, of a spherical indenter tip of radius a into the sample under a controlled applied force, F; the indenter tip is assumed to be perfectly rigid (see sketch in Fig. 2 and Fig. 1 in SI). The measurement location is selected on the surface of a sufficiently large fragment, positioned as far as possible from the edges. During indentation experiments, the specimen is subjected to a vertical load ranging from 0 to a maximum load F_{max} at a rate of 100 μN s^{-1}. Following a holding period of 10s at constant penetration depth, the load is withdrawn at the same rate (Fig. 2).

 This journal is © The Royal Society of Chemistry 2025

Open Access Article. Published on 30 2025. Downloaded on 22/11/25 23:07:05.
This article is licensed under a Creative Commons Attribution 3.0 Unported Licence.

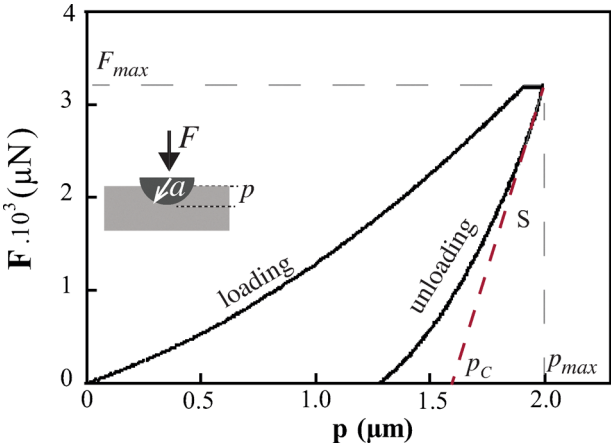

Fig. 2 Load, F, *vs.* penetration depth, p, measured for a nanosilica film dried on a glass substrate (thickness 2×10^3 μm). The radius of the spherical indenter tip is 100 μm. The dashed red line shows the slope S of the unloading part of the load-displacement curve, at maximum penetration depth.

The Young's modulus is extracted from the load–displacement curves using a modified version of the Oliver & Pharr model,[10] adapted for spherical indentation. Specifically, the reduced modulus E_r is determined from the slope S of the unloading curve at the maximum penetration depth, as illustrated in Fig. 2. For a spherical indenter, the projected contact area is calculated as $S_{proj} = \pi a p_c$, where $p_c = p_{max} - \varepsilon \cdot \frac{F_{max}}{S}$ is the contact depth, that accounts for the part of the depth that directly contributes to the projected contact area between the indenter and the material†.[11] The reduced modulus is then computed as: $E_r = \frac{1}{2\beta} \cdot \frac{S}{\sqrt{\pi S_{proj}}}$, where $\beta \approx 1$ is a correction factor accounting for the geometry of the spherical tip. The Young's modulus E is then derived from the reduced Young's modulus by accounting for the elastic modulus of the indenter tip and the corresponding Poisson ratios.[10]

Together, the yield stress, σ_y, of the material can be estimated from nanoindentation testing. The measurements are conducted with a spherical indenter with a radius of 100 μm at a fixed contact penetration depth of 2 μm. Since the films investigated have thicknesses h of 0.5–2 mm, the condition $\frac{\sqrt{pa}}{h} < 10$ is satisfied, ensuring that finite-size effects are negligible during indentation. The yield stress is approximately expresses as $\sigma_y \approx \frac{F_{max}}{C \cdot S_{proj}}$, where C is constraint factor C, typically around 2.8 to 3.0 for ductile materials.[11,12] All measurements were performed three times to ensure reproducibility and to derive error bars.

2.4. Wetting and drying process

In the systematic experiments, we focused on single imbibition/drying cycle. Additional tests were conducted to assess reproducibility over multiple drying/rewetting cycles. For thin films (where the adhesion regions are not circular), up to five cycles were carried out on the same sample, while for thicker films (with circular adhesion regions), up to four cycles were performed. Beyond these numbers, we observed the onset of film degradation, which limited further repetitions. Although we did not perform systematic measurements of the adhesion area at each cycle, we note that the ratio between the adhesion area and the polygonal area remained comparable across cycles.

† ε is a geometric constant ~ 0.75 for spherical tips.

3. Results

3.1. Physical mechanism of delamination during drying

The drying of a silica nanoparticle film leads to the formation of a gel film on the substrate. During this process, various interactions contribute to the film's adhesion to the underlying surface. A key factor governing the adhesion of the film to the substrate is the formation of capillary bridges at the contact points between the gel and the surface. These capillary forces, which arise from the liquid menisci between particles and the substrate, generate strong localized adhesion that anchors the film as it dries. As drying progresses, the gel film undergoes shrinkage due to solvent loss. However, the adhesion to the stiff substrate prevents this contraction, leading to a mechanical mismatch between the film and the substrate. This frustration generates internal stresses within the film, which accumulate as elastic energy during the drying process. The relaxation of this stored energy can lead to mechanical instabilities, such as cracking or delamination, depending on the film's thickness.[13] For films thinner than a critical threshold h_{crack}, the stress remains insufficient to nucleate cracks, and the film remains crack-free. However, above h_{crack}, cracks can form to relieve the stress, leading to a variety of crack patterns. In particular, cracks divide the plane of the film into polygonal cells of surface area, A_0, depending on the film thickness[14] (Fig. 3a). Beyond a value $h_{delamination}$, the delamination of the fragments can take place.

Hence, since each domain dries from a single surface exposed to air, a moisture gradient develops across the film thickness, giving rise to a significant stress gradient (see sketch in Fig. 3b). This gradient induces tensile stress at the surface and compressive stress within the bulk, leading to in-plane compression of the polygonal cells at the drying interface. When the shrinkage-induced stress exceeds a critical threshold, the cells buckle and their edges lift away from the substrate. Adhesion to the substrate further constrains contraction, generating additional in-plane stresses that, once partially released during delamination, amplify the curvature.

Based on energy considerations, delamination occurs when the energy release rate exceeds the adhesion energy. Consequently, delamination initiates at the corners of the domain with angle θ, where stress concentrations arise due to geometric singularities, as illustrated in Fig. 3b.

The temporal evolution of the delamination front, which delimits the boundary between the detached and adhering

Open Access Article. Published on 30 2025. Downloaded on 22/11/25 23:07:05.
This article is licensed under a Creative Commons Attribution 3.0 Unported Licence.

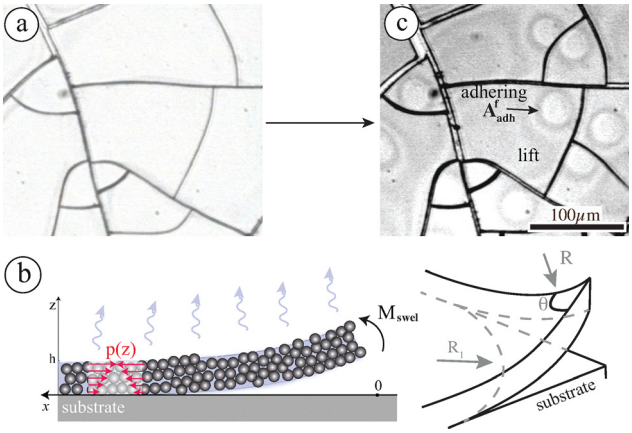

Fig. 3 (a) Crack network dividing the film into polygonal cells (film of nanosilica-Ludox HS40, 50 ± 5 μm thick). (b) Sketch in side view of a delaminated induced by differential drying stress: $p(z)$ is the liquid pressure in the pores, and M is the moment of a force leading to out-of-plane displacement. Sketch exhibiting the delamination of a fragment starting from a corner. (c) Partial delamination observed after crack network formation in image (a), both images were captured using transmitted light optical microscopy.

regions, is clearly visible due to the transparency of the gel, allowing for precise observation (Fig. 4). Together, the plot in Fig. 4 shows the time variations of the dimensionless adhering area, A_{adh}/A_0, and the adhering circularity, C_{adh}, which quantifies morphological changes and deviations from a perfect circular shape, as: $C_{adh} = 4\pi A_{adh}/\ell^2$, where ℓ is the length of the fold which separates the detached region from the adhering one. The process ceases once the adhering region no longer shrinks (Fig. 3c). At this final stage, adhesion to the substrate is limited to a single region of surface area, denoted as A_{adh}^f. The dimensionless final adhering area, A_{adh}^f/A_0, was measured as a function of the initial cell area, A_0, as illustrated in Fig. 5a. Indeed, the last quantity is directly accessible from image analysis. The measurements were performed on a sample with a slight thickness gradient. For small fragments surface area, no delamination is observed (the local thickness is then estimated to be 8 ± 2 μm). As the fragment surface area increases,

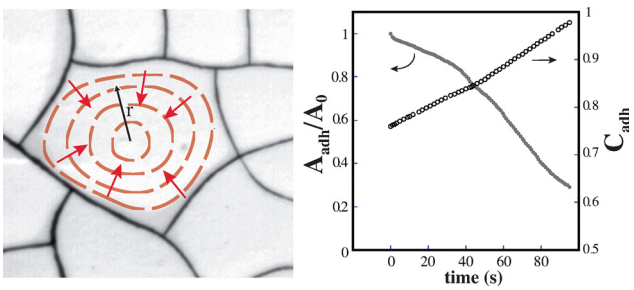

Fig. 4 (Left) Superimposed images illustrating the propagation of the delamination front at successive time intervals of 30 seconds (film of nanosilica-Ludox HS40, 100 ± 5 μm thick). The arrows highlight the progressive shrinkage of the adhering region. (Right) Temporal evolution of the ratio of the adhering area, A_{adh}, to the total cell area, A_0, and the circularity, C_{adh}, of the adhering surface area. The error bars correspond to the size of the data point symbols.

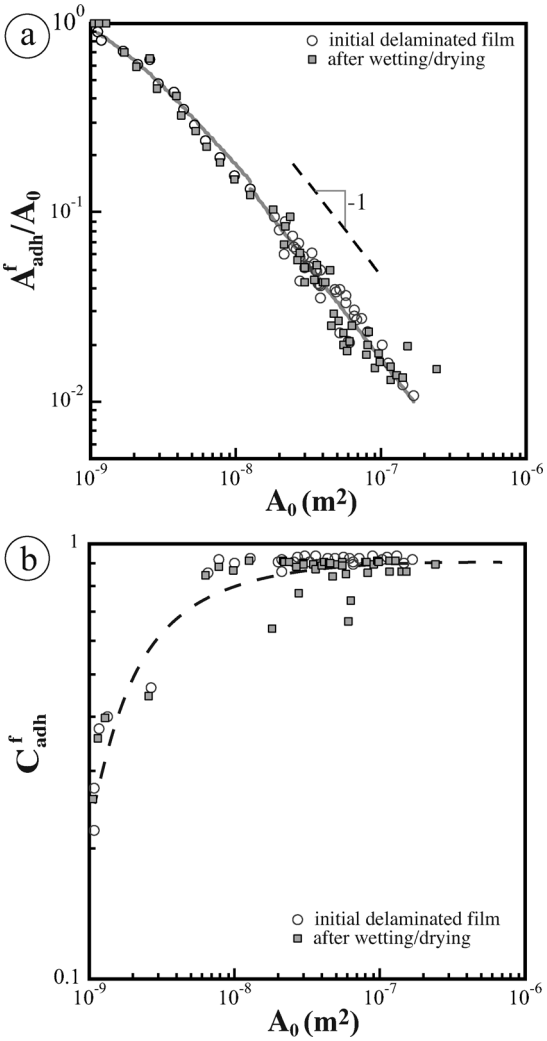

Fig. 5 (a) Log–log plot of the final adhesion ratio, A_{adh}^f/A_0, as a function of the initial fragment area A_0 (films of nanosilica-Ludox HS40). Two conditions are shown: partially delaminated films (○) and films subjected to a wetting/drying cycle (□). The grey line indicates the scaling law predicted by eqn (2) (SI). (b) Circularity C_{adh}^f of the final adhering region, measured from digitized images at the final stage of delamination (the dashed line serves as a visual guide). For both plots, the error bars correspond to the size of the data point symbols.

delamination occurs but remains confined to the edges of the fragments; the adhering region exhibits low circularity that are characteristic of irregular detachment geometries (Fig. 5b). For even larger fragments, delamination becomes progressively more extensive, with film fragments clearly detaching from the substrate. The delaminated fragments maintained a nearly circular adhering region (Fig. 5b). Together, the quantity A_{adh}^f/A_0 decreases inversely with A_0 (Fig. 5a). Note that, as fragment size increases, *e.g.* corresponding to even thicker films, the adhesion areas remain circular, while the ratio of adhered area to total fragment area continues to decrease. However, complete delamination is never observed. The adhered regions maintain mechanical constraints, so curvature is not fully relaxed after drying. Residual curvature persists because the

This journal is © The Royal Society of Chemistry 2025

Open Access Article. Published on 30 2025. Downloaded on 22/11/25 23:07:05.
This article is licensed under a Creative Commons Attribution 3.0 Unported Licence.

colloidal network undergoes plastic or viscoplastic deformation,[15] and irreversible densification ensures that delaminated fragments retain a finite curvature even once moisture is uniform. The theoretical model fails to capture the behavior at large thicknesses, ($h/R > 10\%$, where R is the radius of curvature of the silica fragments), as the thin shell elasticity theory used to estimate the film's bending energy becomes invalid in this regime.

The final adhering surface area results from the minimization of the total energy of the delamination process which expresses as:

$$U_T = U_c + U_b + W, \quad (1)$$

including the bending energy, U_b, of the delaminated film, the drying-induced elastic energy, U_c, and the adhesion energy, W, at the film–substrate interface.

To determine the equilibrium adhering area, A_{adh}^{f}, we differentiate the total energy expression given in eqn (1) with respect to the dimensionless adhering area, $A_{adh}^{f}/A_0 \equiv x^f$ (see SI). By applying the equilibrium condition $dU_T/dx = 0$, we obtain an equation that defines the equilibrium state as:

$$x^f = f(C_{adh}, E, \ldots){A_0}^{-1} \quad (2)$$

This model provides the fitted curve in Fig. 5a.

Two different cases are considered when fitting the experimental data with the model. When the shape of the adhering region deviates significantly from a circle, the circularity values as a function of fragment area are directly incorporated into the bending energy in accordance with Fig. 5b. This scenario corresponds to thinner films, with an experimentally determined thickness of 10 ± 2 μm. When the adhering region is approximately circular, the model assumes a constant circularity across fragment areas.[16] Here, the film thickness used in the model is 30 ± 2 μm, based on experimental measurements. In addition, this energy balance first dictates the onset of the delamination process corresponding to a mimimum value of the fragment size, ${A_0}^{d}$, and so the existence of a critical thickness, $h_{delamination}$, below which the stored elastic energy is not sufficient to overcome adhesion, and delamination does not initiate (Fig. 12 and SI).

While the partially delaminated fragments typically exhibit well-defined adhering surface areas, the location of these adhering regions within each fragment does not follow a systematic pattern. Indeed, the final location of the adhering region, typically exhibiting a preferentially circular shape, is determined by a complex interplay of nucleation and interfacial crack propagation mechanisms. As discussed above, delamination typically initiates at geometrical singularities, following a well-established hierarchy: it begins preferentially at corners, whose influence depends on their opening angle, followed by the edges of the fragments. However, the final position of the adhering region has to take into account the hierarchical crack network that develops during drying, and delays the propagation of the delamination front. This crack network not only limits the extent of the delaminating area but also influences the shape and position of the residual adhered zone.

As fragment size increases, the theoretical model fails to capture the behavior at large thicknesses, $h/R > 10\%$, as the thin shell elasticity theory used to estimate the film's bending energy becomes invalid in this regime.

3.2. Wetting and drying of partial delaminated films

When a partially delaminated film is directly exposed to a liquid, the imbibition process can induce significant macroscopic changes governed by capillary forces. In this way, a pure water droplet with a volume of $v_l \sim 3$ μL is gently deposited on the surface of a partially delaminated film using a micropipette (right region in Fig. 1). In order to prevent detachement of fragments by the liquid deposition, the drop is deposited a few tens of microns from the region observed under the microscope objective. Following deposition, a combination of lateral and vertical liquid flow gradually invades the film and progressively wets the observation region. In particular, capillary pressure, P_c, drives the imbibition of water into the nanoporous network following a diffusive-like law such that the penetration depth increases as:[17]

$$z_{wet}(t) \sim \sqrt{D_p t}, \quad (3)$$

where $D_p \sim kP_c/\eta$ is the effective diffusivity of water in the porous matrix depending on the characteristic permeability, k, and the fluid viscosity, η. Since $D_p \sim 10^{-8}$ m^2 s^{-1} for capillary-driven flow in Ludox-based films, the characteristic time for full-depth imbibition is approximately 1s. Moreover, the imbibed area $\sim v_l/(\phi_p h)$, where ϕ_p is the close-packing particle volume fraction, is of the order of 30 mm^2. Due to the rapid imbibition stage, the liquid remains in contact with the surface of the film, enabling further evaporation process.

The film swelling arises from the imbibition of water into the porous film, generating internal stresses due to hydration and the resulting volume expansion. Since hydration progresses from the exposed surface inward, swelling is non-uniform across the film thickness, resulting in a strain gradient. The local swelling strain is given by:

$$\varepsilon_{swel}(z,t) = \beta C(z,t) \quad (4)$$

where β is a swelling coefficient and $C(z,t)$ is the local water concentration.

Imbibition alters this curvature by inducing in-plane swelling stress, σ_{swel}. This stress arises from the absorption of water into the porous silica matrix, which leads to a local volumetric expansion of the film. Since the wetting process occurs asymmetrically, the swelling is initially non-uniform through the film thickness, generating a mismatch in strain that drives a bending moment as sketch in Fig. 3b. As this swelling mismatch relaxes over time, the initially curved fragment gradually flattens. The internal bending moment responsible for this curvature evolution can be expressed as:[18,19]

$$M_{swel} \sim \sigma_{swel} h^2 \quad (5)$$

Open Access Article. Published on 30 2025. Downloaded on 22/11/25 23:07:05.
This article is licensed under a Creative Commons Attribution 3.0 Unported Licence.

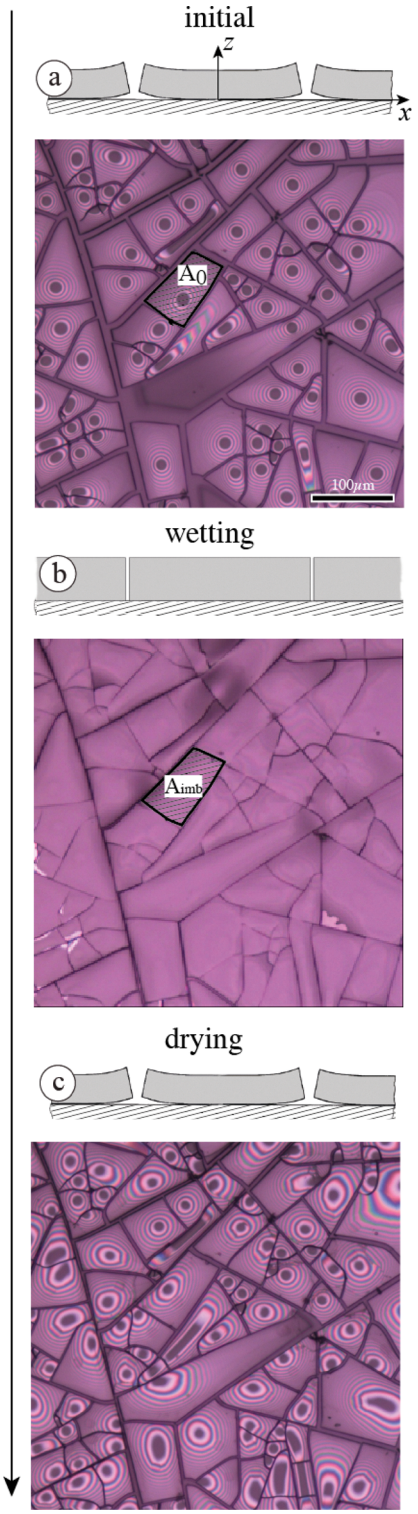

Fig. 6 Sequence of images during the wetting and drying of a film of nanosilica-Ludox HS40, 50 ± 5 μm thick. (a) Sketch in side-view and image of a partially delaminated film. (b) Water deposition on the surface induces imbibition, leading to swelling and subsequent flattening of the fragments. The dashed areas highlights the swelling of a projected surface area of one fragment before, A_0, and after, A_{imb} imbibition. (c) Further drying leads to a subsequent delamination process possibly modifying the location of the adhering regions inside the fragments.

Hence, the film returns to a flat state.

The swelling strain can be quantified by measuring the projected surface area of a fragment before, A_0, and after, A_{imbib}, imbibition (Fig. 6a and b). It comes:

$$\bar{\varepsilon}_{swel} = (A_{imb} - A_0)/A_0 \quad (6)$$

This definition is used here solely as a geometric descriptor of swelling and not as a constitutive strain measure in the sense of linear elasticity. The swelling-induced deformation reaches a maximum value of 26%, based on strain measurements averaged over multiple fragments (see Data Availability Statement).

Although no evidence of crack healing is observed following the imbibition process, re-adhesion of the fragments is apparent from the comparison of the adhering regions before and after the wetting/drying cycle. Indeed, following the swelling induced by imbibition, the subsequent drying step triggers a new delamination process of the fragments. Remarkably, the fragmented pattern remains largely unchanged, with similar adhering surface area (Fig. 7), as pre-existing cracks do not heal during imbibition. In particular, the final relative size of the adhering regions is similar to that observed in the partially delaminated film prior to the wetting/drying cycle (Fig. 5a). Together, the adhering regions exhibit similar shapes (see Fig. 5b). For irregularly shaped regions, with circularity <1, the final adhered area closely matches that observed before wetting. In the case of circular adhesion regions, the final area does not exceed 12% of the fragment area prior to the wetting/drying process.

A key aspect is the location of the adhering region within the fragment. In a film with approximately constant thickness, ±3 μm as estimated by differential focus measurements, the distance, ℓ_{WD}, between the centers of circular adhesion regions before and after the wetting/drying sequence within a fragments were reported in the statistics in Fig. 8. While in some cases the adhered regions remain in approximately the same location, in most cases, a clear positional shift is observed. This observation highlights that a complete re-adhesion of the fragments has occurred between the two delamination processes.

In addition, the curvature of the partially delaminated fragments was assessed using interference fringes observed under reflected light microscopy. These fringes provide a direct optical measure of out-of-plane deformation. Interestingly, the curvature observed after the wetting/drying cycle remains comparable to that measured prior to wetting as shown in the example in Fig. 9. Quantitatively, the curvature radius is on the order of 1 mm, with an average increase of approximately 5–10% relative to the pre-wetting value. These observations support the hypothesis that re-adhesion and subsequent delamination occur under conditions that preserve the film's overall elastic integrity. The mechanisms of re-adhesion can be attributed to the re-establishment of intimate contact between the fragment and the substrate, driven by capillary pressure that promotes water infiltration into the nanoporous silica network. This induces in-plane swelling stress and local volumetric expansion, progressively relaxing the curvature of the fragment. Once contact is restored, van der Waals forces and hydrogen

 This journal is © The Royal Society of Chemistry 2025

Open Access Article. Published on 30 2025. Downloaded on 22/11/25 23:07:05.
This article is licensed under a Creative Commons Attribution 3.0 Unported Licence.

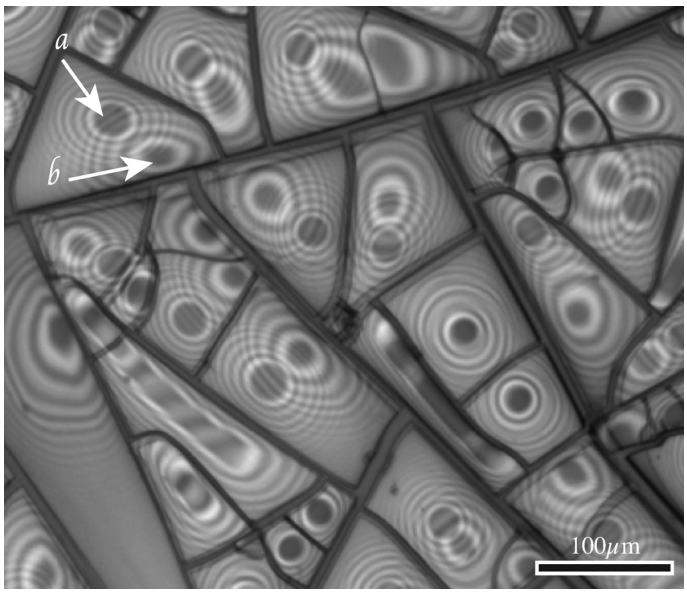

Fig. 7 Addition of two images taken before and after the imbibition/drying process (film of nanosilica-Ludox HS40, 50 ± 5 μm thick). As an example in a given fragment, the adhering region indicated in *a* corresponds to the initial pattern, while the adhering region indicated in *b* is formed after a subsequent wetting and drying process. While the adhesion zones of individual fragments have generally shifted, their overall size remains largely unchanged. The image is 1 mm wide.

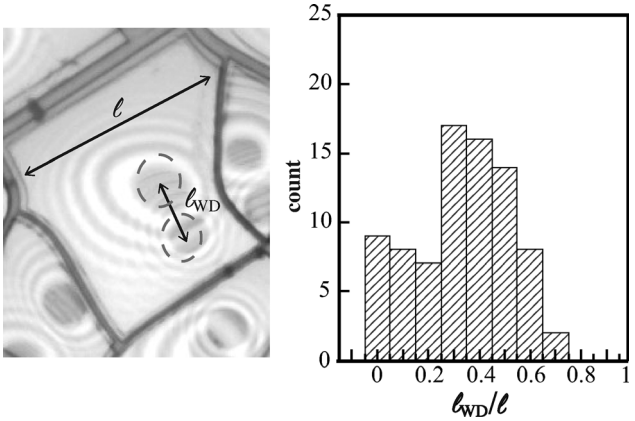

Fig. 8 Statistical comparison of the adhering region location before and after a wetting/drying cycle (film of nanosilica-Ludox HS40, 50 ± 5 μm thick). ℓ_{WD} denotes the length between the two positions, relatively to the characteristic fragment size, ℓ, defined as the square root of its area.

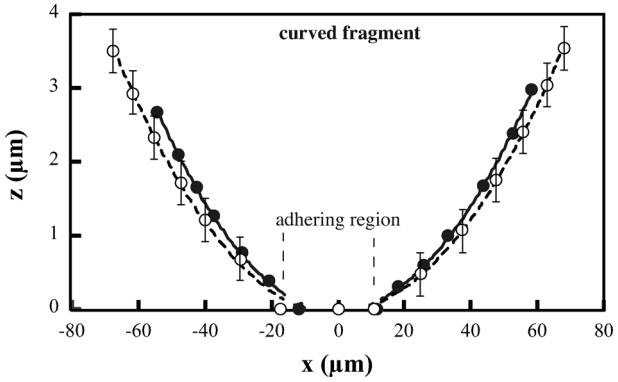

Fig. 9 Profile of a delaminated film fragment before (•) and after (°) a wetting-drying process (film of nanosilica-Ludox HS40, 50 ± 5 μm thick). The error bars, corresponding to the width of the interference fringes, are consistent for both profiles and are shown for only one of them for clarity. The initial curvature results from buckling-driven delamination due to residual drying stresses. The axis correspond to the sketch in Fig. 6a.

bonding stabilize the interface, while substrate roughness or porosity enables mechanical interlocking that further strengthens re-adhesion. Subsequent delamination then arises from the same mechanisms described in the previous section.

3.3. Limitations of interfacial healing

The process described in the previous section has been observed in films formed from various aqueous dispersions of nanosilica (Ludox SM, HS, TM). However, its effectiveness is limited by the intrinsic mechanical properties of the system, which govern the swelling capacity of the porous film. Over time, the films progressively stiffen due to the continued consolidation of the nanoparticle network. This stiffening is evidenced by an increase in the elastic modulus, as measured by nano-indentation for various film thicknesses (Fig. 10a). Specifically, the elastic modulus of nanosilica films increases with time, following a characteristic scaling law with respect to time or particle packing density (lines in Fig. 10a):

$$E(t) \sim E_0 \left(\frac{t}{t_D}\right)^{\alpha}, \quad (7)$$

where E_0 is a reference modulus, $t_D = h/V_E$ is the characteristic drying time depending on the evaporation rate, V_E, and α is a scaling exponent typically around 4 in this system. The evaporation

Open Access Article. Published on 30 2025. Downloaded on 22/11/25 23:07:05.
This article is licensed under a Creative Commons Attribution 3.0 Unported Licence.

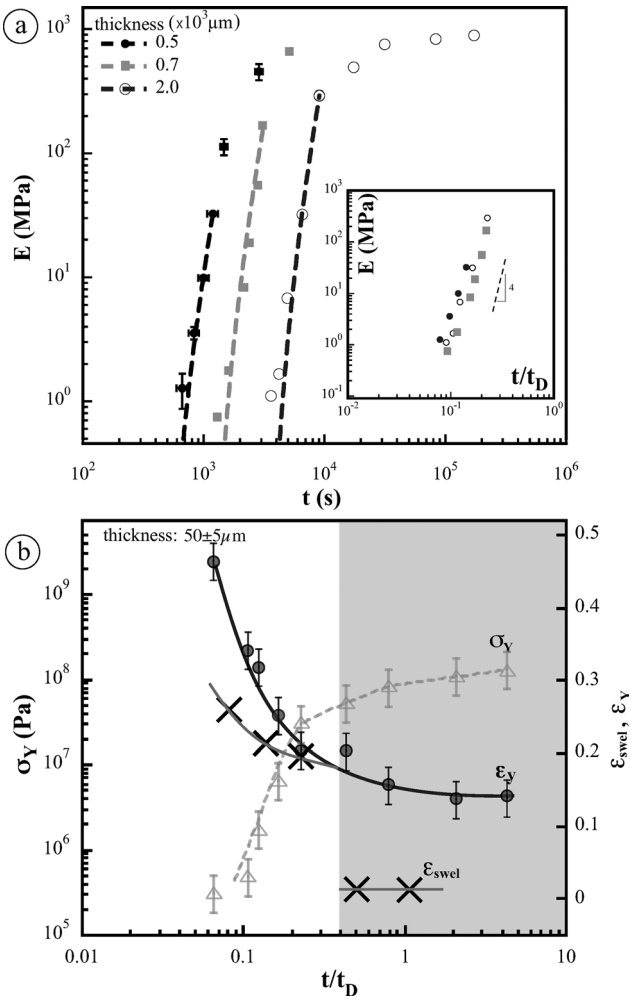

Fig. 10 (a) Evolution of Young's modulus, E, over time for nanosilica films of different thicknesses in a log–log scale. Each data point corresponds to a measurement obtained by nanoindentation using the Oliver and Pharr method. The short-time fits follow a power-law behavior involving a characteristic drying time. Inset: Log–log plot of the elastic modulus as a function of dimensionless time, prior to saturation. The error bars are consistent for all thicknesses and are shown for only one of them for clarity. (b) Yield stress, σ_y (Δ), estimated from nano-indentation on a 2 mm thick film and extrapolated to 50 μm thick film for comparison with the swelling strain, and yield strain, $\varepsilon_y = \sigma_y/E$ (●), plotted as a function of dimensionless time. Swelling strain, ε_{swel} (×), due to imbibition is inferred from fragment surface area measurements for a film of thickness 50 μm. Differences in film thickness arise from fragment size requirements: fragments must be large enough to allow nano-indentation, yet small enough to be observed under the microscope. Since E follows the same scaling law regardless of the characteristic drying time, and thus the film thickness, data extrapolation is justified. The shaded region corresponds to the domain where swelling-induced deformation is negligible, and no re-adhesion process is observed. The lines are guide for the eyes.

rate, V_E, in our experiments is estimated as the rate at which water leaves the porous film into the surrounding air. Under the experimental conditions, the water loss is the diffusion of water vapor through the boundary layer of air above the film.

Note that, contrary to the classical definition of drying time, t_D, the thickness, h, involved refers here to the structured solid film rather than the initial liquid film just after deposition, as this solid thickness can be directly measured.

Eqn (7) captures the sharp increase in stiffness as the film solidifies and interparticle contacts evolve to support mechanical loads. This trend is independent of film thickness, as highlighted by the collapse of the measurements when the elastic modulus is plotted as a function of dimensionless time (see inset in Fig. 10a).

This time increase of the film stiffness is consistent with earlier observations in sol–gel systems.[20] In general, one of the primary mechanisms responsible for this time-dependent stiffening is the progressive condensation of silanol (Si–OH) groups into siloxane (Si–O–Si) bonds, which increases the connectivity of the nanoparticle network. This process leads to enhanced rigidity as the network becomes more extensively cross-linked.[20,21] In addition to chemical condensation, physical densification also contributes to the increase in Young's modulus. Recent studies further suggest that this mechanical stiffening is not solely due to densification, but also arises from the progressive formation of interparticle bonds. In particular, Bonacci *et al.*[22] demonstrated that aging in nanosilica gels leads to condensation reactions at particle contacts, strengthening the network over time. This process enhances the mechanical integrity of the film by increasing the connectivity and strength of the colloidal network, offering a microscopic origin for the observed macroscopic stiffening. After a period of time, the rate of stiffening slows down. This saturation behavior corresponds to the final stage of drying, during which the film has largely lost its free water. In parallel with this increase in stiffness, we also observe a decrease in the yield strain as the film ages (Fig. 10b). This reduction highlights the progressive loss of the film's ability to undergo plastic deformation or accommodate swelling upon water imbibition.

Hence, as the film becomes mechanically stiffer over time, its ability to swell in response to water imbibition progressively diminishes. This reduction in swelling capacity is quantified by the swelling strain, calculated using eqn (6). As shown in Fig. 10b, the swelling strain decreases with time, reflecting the reduced capacity of deformation of the consolidating nanoparticles matrix. Together, measurements using nanoindentation testing show that the yield stress of the material increases over time. Combined with the evolution of the elastic modulus, this indicates that the yield strain, $\varepsilon_y = \sigma_y/E$, decreases with time (Fig. 10b). These measurements of the elastic modulus and yield stress were performed on solid films with a thickness of 2 mm. To estimate the temporal evolution of these mechanical properties for thinner films, below the experimentally accessible range, we extrapolated the data using the characteristic drying time t_D. This trend highlights the diminishing capacity of the material to undergo elastic deformation during imbibition. When the swelling strain reaches the yield strain, the film can no longer accommodate the swelling stress elastically, and further deformation is inhibited. In this regime, the flattening of initially curved, partially delaminated fragments becomes mechanically blocked. This limitation is illustrated by the shaded region in Fig. 10b, which delineates the

 This journal is © The Royal Society of Chemistry 2025

Open Access Article. Published on 30 2025. Downloaded on 22/11/25 23:07:05.
This article is licensed under a Creative Commons Attribution 3.0 Unported Licence.

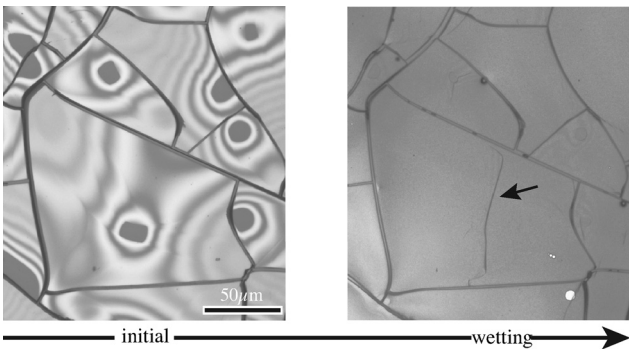

Fig. 11 Starting from a partially delaminated film, imbibition can induce the formation of new cracks within the fragments when the film is sufficiently brittle as the one indicated by the black arrow.

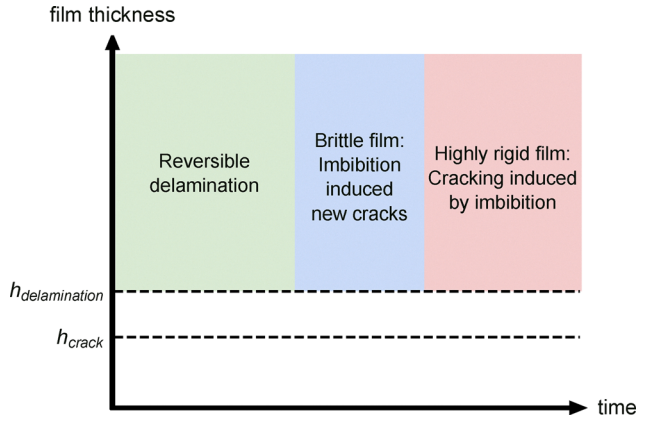

Fig. 12 Diagram of film response after imbibition as a function of time and film thickness.

domain where swelling-induced re-adhesion is no longer possible. This interplay between increased stiffness and reduced deformability of the film underscores the importance of time-dependent mechanical evolution.

Hence, the swelling-induced deformation becomes negligible and correlates with the emergence of the film's brittle properties. The time at which this deformation significantly decreases can be estimated from the measurements of ε_{swel} and is indicated in Fig. 10b. Togeteher, in rigid films, imbibition can even directly lead to cracking (Fig. 11). This occurs because capillary pressure generated during liquid infiltration into nanopores can induce large internal stresses. While soft films can relax these stresses through elastic deformation, rigid films cannot, and when the capillary-induced stress exceeds the fracture strength of the material, cracking occurs.

This transition can be accelerated by increasing the film's temperature. Typically, placing the film in an oven at 60 °C for a few minutes is sufficient to remove residual water from the nanopores. Upon cooling, subsequent imbibition by water leads to cracking of the film.

4. Conclusion

The drying of nanosilica films typically results in a characteristic crack network that divides the surface into discrete fragments. The evolution of these mechanical instabilities, such as cracking and delamination, is strongly influenced by both the film thickness and the drying time, as summarized in the diagram in Fig. 12. In particular, delamination tends to occur when the film thickness exceeds a critical threshold, and its onset is further modulated by the temporal dynamics of stress development during drying. These delaminated fragments exhibit well-defined adhesion regions, and remarkably, the process is reversible: surface wetting induces imbibition, which triggers curvature relaxation, and progressive reattachment to the substrate. A subsequent drying cycle gives rise to a new pattern of partial delamination. Although the size of the adhesion zones remains largely unchanged, their positions often shift, revealing that re-adhesion during swelling involves interfacial healing between the film and the substrate. This reversibility is effective in films that maintain sufficient elasticity. In contrast, films that are too stiff, or brittle, tend to fracture during swelling, preventing reattachment. The phenomenon is reproducible across various types of silica, provided the material is ductile enough to accommodate the mechanical stresses induced by swelling. At this stage, moving beyond the current model system offers a promising way to study similar re-adhesion mechanisms in films made of anisotropic nanoparticles, such as aluminosilicate particles.

Author contributions

C. H.: investigation, writing – review editing. J.-P. R.: writing – review editing. L. P.: visualization, investigation, formal analysis, writing – original draft, writing – review editing.

Conflicts of interest

There are no conflicts to declare.

Data availability

Raw data generated and analyzed in this article are available at the following URLs: **https://sdrive.cnrs.fr/s/H9LHQX6Z6jEmarH**, **https://sdrive.cnrs.fr/s/dCPtZZtCcQMiTCa**, **https://sdrive.cnrs.fr/s/j8pcwEgqMf2NNCs**, **https://sdrive.cnrs.fr/s/82Yj75WipGijE4t**. For any additional datasets or information, please contact the corresponding author.

Supplementary information (SI) is available. See DOI: **https://doi.org/10.1039/d5sm00750j**.

Acknowledgements

We are grateful to J. Amarni, A. Aubertin, L. Auffray, C. Manquest and R. Pidoux for their contribution to the development of the experimental setup.

Open Access Article. Published on 30 2025. Downloaded on 22/11/25 23:07:05.
This article is licensed under a Creative Commons Attribution 3.0 Unported Licence.

Notes and references

1 J. Sarkar and M. S. Tirumkudulu, *Soft Matter*, 2011, **7**, 6382–6397.
2 B. Sobac, P. Colinet and L. Pauchard, *Soft Matter*, 2019, **15**, 2381–2390.
3 M. F. Osman, L. Zou, L. Pauchard and F. Giorgiutti-Dauphiné, *Soft Matter*, 2020, **16**, 8345–8351.
4 R. P. Berkelaar, P. Bampoulis, E. Dietrich, H. P. Jansen, X. Zhang, E. S. Kooij, D. Lohse and H. J. W. Zandvliet, *Langmuir*, 2015, **31**, 1017–1025.
5 Z. Xia and J. Hutchinson, *J. Mech. Phys. Solids*, 2000, **48**, 1107–1131.
6 S. Perumanath, R. Pillai and M. K. Borg, *Nano Lett.*, 2023, **23**, 4234–4241.
7 A. Pandey and D. P. Holmes, *Soft Matter*, 2013, **9**, 5524–5528.
8 L. Pauchard, *Phys. Fluids*, 2023, **35**, 067107.
9 T. Young, *Philos. Trans. R. Soc. London*, 1805, **95**, 65–87.
10 W. Oliver and G. Pharr, *J. Mater. Res.*, 1992, **7**, 1564.
11 A. C. Fischer-Cripps, *Nanoindentation*, Springer, New York, 2011.
12 E. Di Giuseppe, A. Davaille, E. Mittelstaedt and M. François, *Rheol. Acta*, 2012, **51**, 451–465.
13 V. Lazarus and L. Pauchard, *Soft Matter*, 2011, **7**, 2552–2559.
14 X. Ma, J. Lowensohn and J. C. Burton, *Phys. Rev. E*, 2019, **99**, 012802.
15 H. Lama, L. Pauchard, F. Giorgiutti-Dauphine and S. Khawas, *Phys. Rev. Mater.*, 2023, **7**, 025604.
16 L. Pauchard, *Europhys. Lett.*, 2006, **74**, 188–194.
17 E. Washburn, *Phys. Rev.*, 1921, **17**, 273.
18 R. W. Style, S. S. L. Peppin and A. C. F. Cocks, *J. Geophys. Res.: Earth Surf.*, 2011, **116**, F01025.
19 F. Giorgiutti-Dauphiné and L. Pauchard, *Colloids Surf., A*, 2015, **466**, 203–209.
20 C. Brinker and G. Scherer, *Sol-Gel Science: The Physics and Chemistry of Sol-Gel Processing*, Academic Press, New York, 1990.
21 J. Dziadkowiec, H.-W. Cheng, M. Ludwig, M. Ban, T. P. Tausendpfund, R. von Klitzing, M. Mezger and M. Valtiner, *Langmuir*, 2022, **38**, 6949–6958.
22 F. Bonacci, X. Chateau, E. M. Furst, J. Fusier, J. Goyon and A. Lemaître, *Nat. Mater.*, 2020, **19**, 775–780.

This journal is © The Royal Society of Chemistry 2025